SCIENTIFIC REPORTS

OPEN

SUBJECT AREAS:
PERMEATION AND TRANSPORT
NEPHRONS
OPTICAL IMAGING
MEMBRANE BIOPHYSICS

Received
17 December 2012

Accepted
4 September 2013

Published
25 September 2013

Correspondence and requests for materials should be addressed to Y.S. (yoshiros@med.keio.ac.jp)

* These authors contributed equally to this work.

Direct visualization and quantitative analysis of water diffusion in complex biological tissues using CARS microscopy

Ying-Chun Yu[1]*, Yoshiro Sohma[1]*, Shinichi Takimoto[2], Takayuki Miyauchi[1] & Masato Yasui[1]

[1]Department of Pharmacology, Keio University School of Medicine, Tokyo, Japan, [2]Medical Technology R&D Division, Olympus Corporation, Tokyo, Japan.

To date, it has not been possible to measure microscopic diffusive water movements in epithelia and in the interstitial space of complex tissues and organs. Diffusive water movements are essential for life because they convey physiologically important small molecules, e.g. nutrients and signaling ligands throughout the extracellular space of complex tissues. Here we report the development of a novel method for the direct observation and quantitative analysis of water diffusion dynamics in a biologically organized tissue using Coherent Anti-Stokes Raman Scattering (CARS) microscopy. Using a computer simulation model to analyze the CARS O-H bond vibration data during H_2O/D_2O exchange in a 3D epithelial cyst, we succeeded in measuring the diffusive water permeability of the individual luminal and basolateral water pathways and also their response to hormonal stimulation. Our technique will be applicable to the measurement of diffusive water movements in other structurally complex and medically important tissues and organs.

Recent advances in nonlinear optical microscopy have allowed researchers to determine the chemical composition of living cells and organisms[1]. Coherent Anti-Stokes Raman Scattering (CARS) laser-scanning microscopy is a type of nonlinear optical microscopy that produces an image of signals originating from the vibration energy of inter-atomic bonds in molecules, e.g. the C-H bond vibration for imaging lipids. The development of high-performance CARS microscopy in the early 21st century[2,3], was followed by development of the background-free, stimulated Raman scattering (SRS) imaging microscope[4] and the improved coherent Raman scattering (CRS) microscope[5,6]. These non-linear optical techniques have been used by cell biologists for several years; however, most studies have focused on observing C-H bond vibrations, because it provides information on the localization of organic substances that constitute biologically important molecules[7]. Early on in the development of CARS microscopy, Potma *et al.*[8] reported that observation of the O-H bond vibration could be used to visualize the intracellular diffusion of H_2O in the amoebozoa if the extracellular medium was rapidly switched from an H_2O-based to a deuterated water (D_2O) –based solution. However, after this initial physical study[8], the CARS technique has not been used to investigate diffusive water movements in organized biological tissues.

Following the discovery of aquaporin (AQP) water channels in 1992[9], water homeostasis has become an important field in the biomedical sciences. To date, thirteen subtypes of AQPs have been identified in mammals. These AQPs can be separated into two main groups on the basis of their permeability characteristics: the aquaporins (e.g., AQP1, AQP2, AQP4) and the aquaglyceroporins (e.g., AQP3, AQP7, AQP9)[10,11]. Some of these AQPs are expressed in the renal system, making it a good organ system in which to address questions about the role played by AQPs in water homeostasis.

The membrane transport processes that orchestrate secretion and absorption by epithelia are essential for life. Abnormalities in membrane transport mechanisms underlie common human diseases in the gastrointestinal, respiratory and reproductive systems, and understanding them is key to developing new therapeutic strategies[10]. In the past, most studies have targeted the transport mechanisms for the solute rather than the solvent water due to the lack of a method for directly measuring water diffusion processes. Although the net osmotic water flux driven by an osmolality difference can be estimated by measuring the volume of water moved, e.g. through either changes in cell volume or the volume of secreted fluids, the details of isotonic diffusive water fluxes (i.e. water flux

without any net volume movement), as well as the permeation pathways involved, have not been available[12]. These diffusive water fluxes are important for distributing biological molecules around the extracellular space of tissues and the CARS technique provides a methodology for studying them.

Since we established our CARS microscopy system and confirmed its reliability using single mammalian cells[13], we have developed a novel strategy to characterize the dynamics of water diffusion in complex biological tissues. In the current study, we applied the CARS technique to epithelial 3D cysts formed by Madin-Darby canine kidney (MDCK) cells[14] and renal cortical collecting duct (CCD)-origin M-1 cells[15] and succeeded in directly observing H_2O/D_2O exchange across the epithelial cysts. We analyzed the time-lapse image data with a novel computer simulation model and succeeded in determining the diffusional water permeabilities of the luminal and basolateral membranes, and their response to hormonal stimulation. This is the first report of the direct visualization of diffusional water movement across an epithelium (an important structural component in many complex biological tissues), together with the determination of the diffusional water permeabilities of the luminal and basolateral membranes in real time.

Results

Principles of the direct measurement of water diffusion across an epithelium using CARS microscopy. We mounted cysts buried in a thin Matrigel layer on the inverted CARS microscope, which was developed in cooperation with the Olympus Corporation (**Fig. 1A**). All the experiments were performed on cysts with an almost perfect spherical shape and formed by epithelia of uniform thickness. CARS microscopy gives us confocal images because it is a four-wave mixing process which occurs probabilistically only at the focal point[2,3], which was the plane through the center of the cyst (**Fig. 1A**). Figure 1B shows a multi-shelled, three compartment, model developed to estimate the water permeability of the luminal and basolateral membranes of the cysts from the CARS H_2O images (signal intensity) using the H_2O/D_2O exchange technique (see supplement for details). To derive the H_2O concentration from the CARS H_2O signal intensity, we measured the CARS H_2O signal intensity of solutions containing various H_2O/D_2O ratios (**Fig. 1C–i**), and obtained a calibration curve for the relationship between the normalized CARS H_2O signal intensity and the normalized H_2O concentration (**Fig. 1C–ii**) (See **Methods** and **Supplementary Methods** for more detail).

Figure 2 shows immuno-histochemical staining of cysts formed by WT-MDCK cells. The 3D structure of the cell membrane (stained by α−tubulin) and the nuclei (stained by Hoechst 33258) indicate that WT-MDCK cells formed a cyst with a single layer of epithelium. Also the network of pentagonal and hexagonal frames stained by ZO-1 suggest that the tight junction is correctly formed between the MDCK cells (**Fig. 2A**). Figure 2B-i shows a fluorescent image of a WT-MDCK cyst 30 min after the application of 4-kDa FITC-dextran (leak test). No luminal FITC signal was observed for 30 min after the FITC-dextran was added to the bath solution (**Fig. 2B–ii**), suggesting that this cyst had formed functional tight junctions.

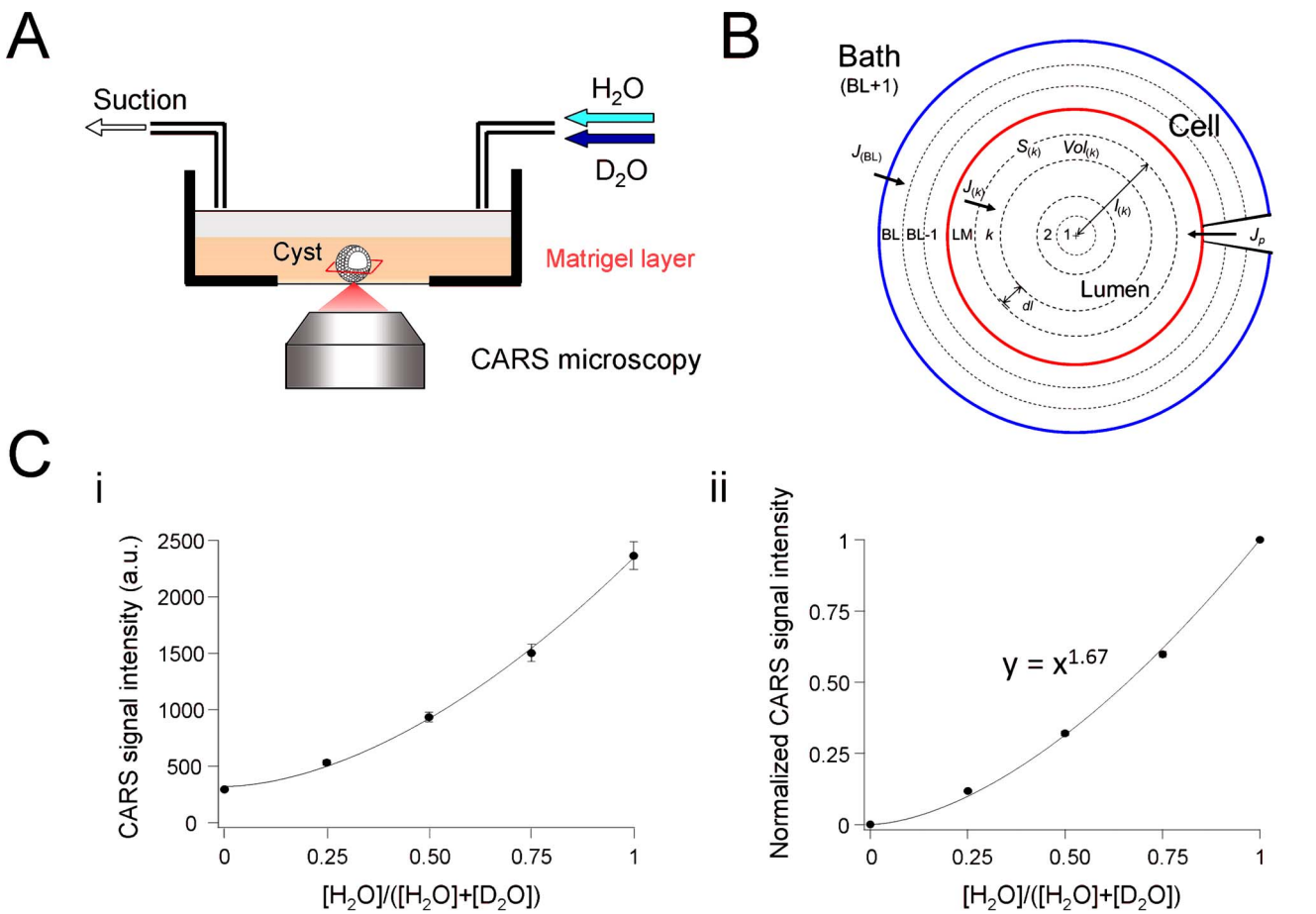

Figure 1 | Experimental set-up and analysis model. (A) Set-up for the H_2O/D_2O exchange experiment on the CARS microscopy stage. (B) Multi-shelled three compartments model for analyzing the H_2O/D_2O exchange data. LM and BL are the numbers of the most-outside shell compartment representing lumen and cell. See the supplementary method for more detail. (C) Property of CARS signal obtained from mixtures of H_2O and D_2O. **(i)** Raw CARS signal intensity obtained from H_2O/D_2O mixtures with a various different ratios. n = 3. **(ii)** The calibration curve for the relationship between the H_2O concentration and the normalized CARS signal intensity. Derived from the raw CARS signal intensity shown in Fig. 1C–i.

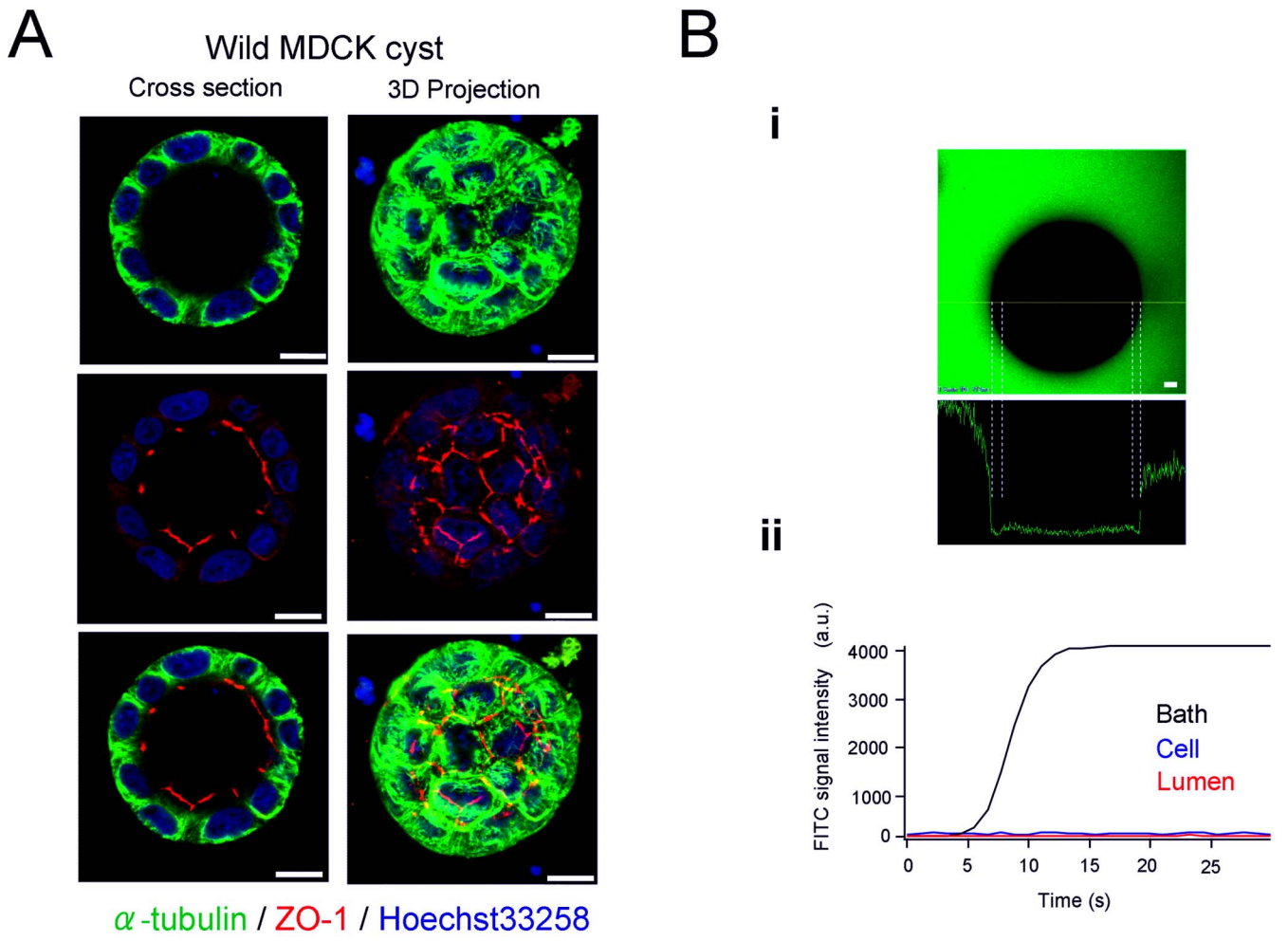

Figure 2 | **Complete cyst formation by WT-MDCK cells.** (A) Cross section and 3D projection images of immuno-histochemical stained cysts from WT-MDCK cells (Day 5). (green) α-tubulin; (red) ZO-1; (blue) Hoechst33258. The scale bars indicate 10 μm. (B) Representative example of a leak test in WT-MDCK cysts. **(i)** A fluorescent image of a WT-MDCK cyst 30 min after the application of 1 ml 4-kDa FITC-dextran (5 mg/ml) with the intensity profile of the FITC fluorescent signal across the MDCK cyst. **(ii)** Time-course of the FITC signals in bath and lumen after the FITC-dextran application.

Direct observation of H_2O/D_2O exchange and estimation of water permeability in the MDCK epithelial cysts. With the control H_2O-based solution, the CARS H_2O-signal imaging showed double low density rings in which the inner and outer rings (**Fig. 3A**) represented the luminal and basal membranes of the epithelium forming the cyst (**Fig. 2A**). The intracellular area of the epithelial layer was observed as a homogenous space in which the signal intensity was either comparable, or slightly less than, that in the bath and lumen, which might be due to the intracellular organelles.

On switching the bath perfusion solution from the H_2O- to D_2O-based one, the CARS signal intensity in the bath was reduced to the level of the D_2O- based solution virtually homogenously within a few seconds (**Fig. 3A**, also see **Supplementary Video 1**). Following this signal reduction in the bath, the CARS signal intensity in the cell layer and then in the lumen were reduced to the level of the D_2O-based solution. Note that the H_2O/D_2O exchange is a passive process and occurred in the absence of an osmotic gradient.

The relative time course of the signal intensity changes in the intracellular area was unclear because of the slower time resolution (~1.1 sec/frame) in the 2D imaging (**Fig. 3A**). To obtain a better time-resolution (~ 0.5–1.2 ms/line), we performed the CARS signal measurement in the line-scanning mode (**Fig. 3B**). To minimize possible artifacts, we chose an area showing clear and homogenous CARS H_2O signals to avoid any signal scattering caused by the 3D shape of the cysts (**Fig. S7**).

Estimation of water permeability from CARS H_2O signal intensity. Figure 4A shows the relaxations in the CARS signal intensity at representative points in the bath, cell and lumen respectively, following the H_2O to D_2O perfusion switch. The cellular and luminal CARS signals were decreased following the fall in the bath signal intensity. Because the CARS H_2O signals recorded from the intracellular compartment close to the basal membrane were of low amplitude and noisy, we chose to record from a point away from the basolateral membrane which exhibited a clear signal.

Because the CARS signal relaxations will be affected by the geometry of the cyst as well as the permeability of the water pathways, we employed a mathematical modeling approach to analyze the data based on the best fit to a multi-shelled, three compartment, model to estimate the water permeability (see **Methods**). The cellular and luminal CARS signal relaxations were well-fit by the curves generated from the experimental CARS signal intensity data in the cyst simulation model (solid lines in **Fig. 4B**), which allowed us to estimate the water permeabilities of the luminal and basolateral membranes in the cyst. The diffusive water permeabilities, P_d, in the luminal and basolateral membranes were estimated to be $1.2 \pm 0.2 \times 10^{-3}$ cm/s and $2.4 \pm 0.4 \times 10^{-3}$ cm/s respectively (also see **Fig. 7E**). Using this model for analysis also suggested that the paracellular pathway did not contribute to the diffusive movement of water in the MDCK cysts, which is consistent with a previous report

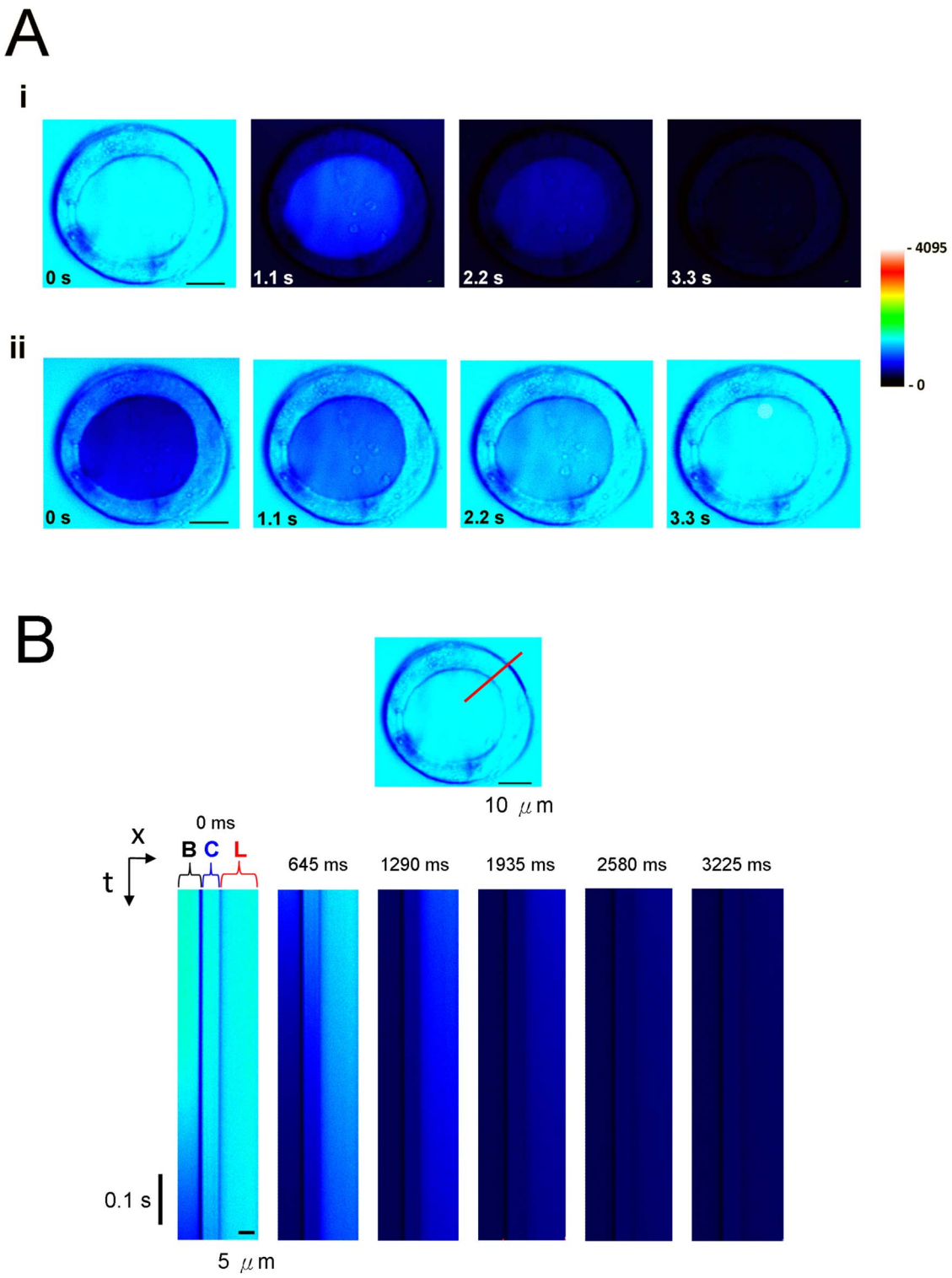

Figure 3 | Direct observation of the H_2O/D_2O exchange process in a MCDK cyst using CARS microscopy. (A) CARS x-y scanning images of a MDCK cyst during the exchange **(i)** from H_2O to D_2O and **(ii)** from D_2O to H_2O. Scale bar: 10 μm. 512 × 512 pixels. Also see **Supplementary Video 1**. (B) CARS line scanning data in the MDCK cyst during the exchange from H_2O to D_2O. 266 × 2015 pixels. 0.103 μm/pixel; 1.6 ms/line.

that cultured MDCK monolayers had a negligible 'osmotic' water permeability across the tight junctions[16]. Note that complete cyst formations were confirmed using FITC-dextran (**Fig. 2B**).

Reproducibility of the H_2O/D_2O exchange experiment. To check the reproducibility of the experiments, we measured the CARS H_2O signal intensity of a MDCK cyst during repeated H_2O/D_2O exchanges (**Fig. 5**). The decays of the CARS signal intensity in the lumen and the cell following that in the bath were very similar over the three repeats of the H_2O/D_2O exchanges (**Fig. 5–i, ii, iii**), which suggests that the experimental method is reliable and that there was minimal photodamage to the cysts under our experimental condition.

Comparisons of the H_2O to D_2O and the D_2O to H_2O switching protocols in estimating the water permeability values. We made

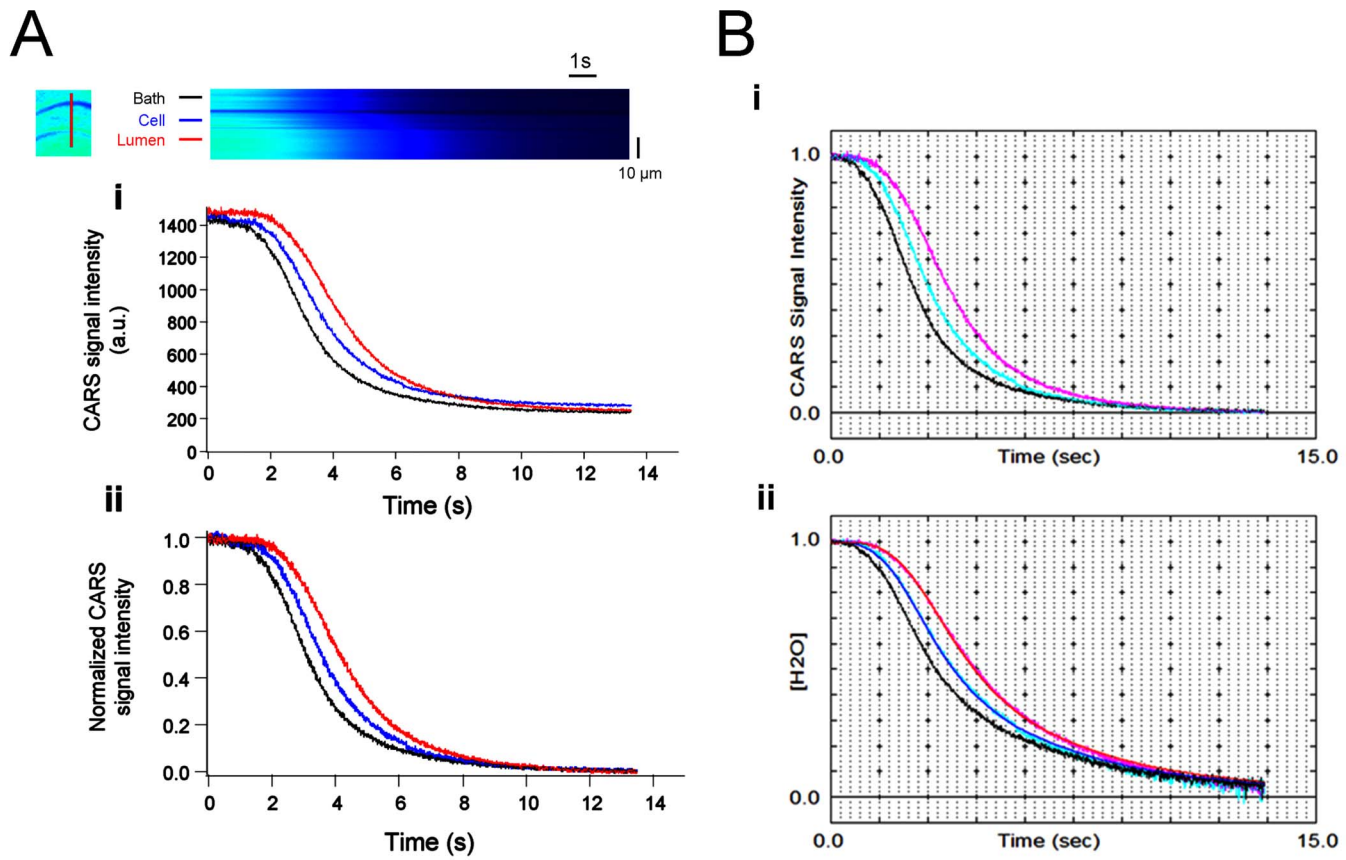

Figure 4 | Procedure for estimating the water permeability from the CARS [H2O] signal intensity data. (A) Normalization of the sequential CARS [H_2O] signal intensity data at representative points in the bath (black), cell (blue) and lumen (red) in the MDCK cyst following the H_2O to D_2O perfusion switching. **(i)** Raw and **(ii)** normalized sequential CARS [H_2O] signal intensity data are shown. (Top panel) CARS line scanning data. 120 × 10385 pixels. 0.301 μm/pixel; 1.3 ms/line. See the supplement for the method for normalizing the data in detail. (B) Determination of water permeability from the CARS signal intensity data by the analysis program based on the multi-shelled three compartments model. **(i)** Input: the normalized CARS signal intensity input to the analysis program. **(ii)** Output: the normalized H_2O concentration data calculated from the normalized CARS signal intensity data input. The best-fit curves generated by the multi-shelled three compartments model were superimposed with the experimental luminal and cellular [H_2O] data. See Supplementary Methods for more detail.

comparisons between the water permeability values estimated from the signal decay induced by switching the H_2O-based solution to the D_2O-based solution and the signal recovery induced by switching back from the D_2O-based solution to the H_2O-based solution (**Fig. 6**).

Figure 6A shows a representative trace of the raw CARS H_2O signal intensity data obtained by switching from H_2O to D_2O and the sequential switch back from D_2O to H_2O. After the normalization of the CARS signals for at each part of the experiment (**Fig. 6B**), the $P_d(l)$ and $P_d(bl)$ values were estimated (**Fig. 6C**). Note that the $P_d(bl)$ values were the same when measured on the H_2O to D_2O switch and the D_2O to H_2O switch back (**Fig. 6D**). In contrast, $P_d(l)$ values estimated using the two protocols were significantly different with the H_2O to D_2O switch giving the higher value. (**Fig. 6D**). The reason for this protocol-related difference in $P_d(l)$ is unclear; however, we noticed that the cysts used in these experiments could be divided into two groups. In one group, comprising the majority (75%) of cysts, $P_d(l)$ was not significantly different when measured on the H_2O to D_2O switch and *vice versa* (**Fig. S9**). In contrast, cysts in the second group, comprising 25% of the total, exhibited a significant difference in $P_d(l)$ between the two protocols. We can only speculate as to why $P_d(l)$ would vary in this way in some cysts, but it might reflect rapid regulation of luminal diffusive water permeability and/or heterogeneity of the MDCK cells. Importantly, the fact that the majority of cysts did not exhibit a protocol-related difference in $P_d(l)$ suggests that an experimental artifact is not the explanation. Note that we consistently employed the H_2O to D_2O switch in all further experiments in which P_d values were measured (see below).

Effects of stable transfection of the AQP4 on water permeability of MDCK epithelia. Next we measured water movement in mouse AQP4 (mAQP4)-stably transfected MDCK cysts (**Fig. 7**). The mAQP4 –MDCK cysts were also confirmed as being formed by a single layer of epithelium with tight junctions (**Fig. 7A**). AQP4 has been reported to be expressed on the basolateral membrane of renal and airway epithelia[10,11]. In the MDCK cysts, immuno-staining showed that transfected mAQP4 was localized to the basolateral membrane (**Fig. 7B–i**) and the cysts expressing mAQP4 could be identified by the co-transfected EGFP signal (**Fig. 7B–ii**). The H_2O/D_2O exchange experiment performed on mAQP4-MDCK cysts (**Figs. S8**), followed by the leak test (**Fig. 7C**), showed that the fall in the intracellular CARS signal was relatively faster in the mAQP4-MDCK cysts (**Figs. 7D**) compared to WT-MDCK cysts (**Fig. 4B**), whereas the relaxation of the luminal CARS signal was not significantly different (**Fig. 7D**).

Figure 7E shows a summary of the luminal and basolateral diffusive water permeability P_d in WT- and AQP4-MDCK cysts. The simulated analysis showed that the basolateral diffusive water permeability P_d in AQP4-MDCK cysts was ~3–4 -fold higher than in

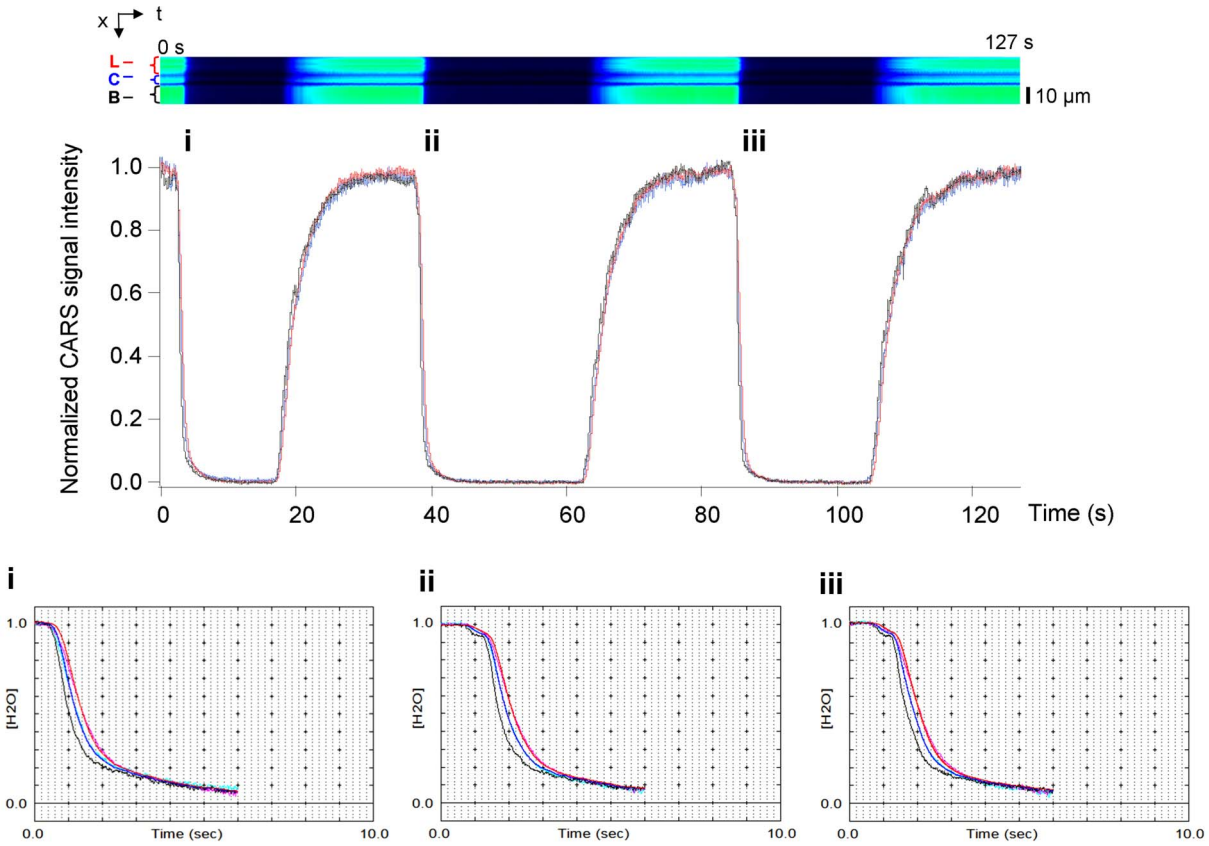

Figure 5 | Reproducibility of the H_2O/D_2O exchange experiment. A continuous recording of the CARS signal intensity obtained during the three repeat H_2O/D_2O exchanges in the lumen (red), cell (blue) and bath (black) compartments (upper panel). 130 × 31750 pixels. 0.414 μm/pixel; 4 ms/line. The insets (i) – (iii) show the expansions of the $[H_2O]$ decays in luminal, cell and bath superimposed with the best-fit curves generated by the analysis program. $P_d(l)$: (i) 4.3×10^{-3} cm/s, (ii) 4.2×10^{-3} cm/s, (iii) 4.3×10^{-3} cm/s. $P_d(bl)$: (i) 4.7×10^{-3} cm/s, (ii) 4.4×10^{-3} cm/s, (iii) 4.9×10^{-3} cm/s.

the WT-MDCK cysts. In contrast, the luminal diffusive water permeability in mAQP4-MDCK cysts was the same as that observed in WT-MDCK cysts (**Fig. 7E**). This is consistent with the basolateral localization of mAQP4 in the transfected MDCK cysts (**Fig. 7B**).

Direct measurement of the effects of vasopressin on water permeability in the M-1 epithelia. Finally, we attempted to observe a physiologically important, hormone-induced, change in water permeability in an intact epithelium. We made cysts from M-1 cells derived from the mouse cortical collecting duct (CCD), which has been used as a mammalian model of the CCD[15]. It has been reported that while AQP2 is largely restricted to intracellular vesicles in the basal state, vasopressin induces a redistribution of AQP2 to the apical membrane of the CCD[15,17]. Immunostaining showed that the M-1 cysts expressed AQP2 in the cytosol with a coarse-grained pattern in the control, unstimulated, condition (**Fig. 8A**). Application of arginine-vasopressin (AVP) caused AQP2 expression to appear on the luminal membrane in the M-1 cysts (**Fig. 8A**), consistent with a previous report[17]. In these experiments, we confirmed the complete formation of M1-cysts by the leak test (**Fig. 8B**).

We measured the diffusive water permeability, P_d, of the M-1 cysts before and after the AVP application (**Fig. 8C**). Consistent with the immunostaining data (**Fig. 8A**), AVP application increased the luminal water permeability, $P_d(l)$, by ~50% whereas no significant change in the basolateral P_d (bl) was observed (**Fig. 8D**).

Discussion

The transporting epithelium is an important component in both the structural and functional organization of complex biological tissues. In the present study, we report the first application of CARS microscopy to a structured biological tissue (i.e. an epithelium), which has allowed, also for the first time, the measurement of the diffusive water permeability P_d of the luminal and basolateral epithelial cell membranes.

In WT-MDCK cysts, the diffusive water permeability P_d of the basolateral membrane was estimated to be ~2-fold higher than that of the luminal membrane. This is partially due to the area of the basolateral membrane being larger than that of the luminal membrane (see **Supplementary Methods**). Making the simple assumption that MDCK cells forming the cyst have a cuboidal shape, the area of basolateral membrane was estimated to be 5-fold larger than that of the luminal membrane. The close contacts between the cells at their lateral faces (**Fig. 2A**) should reduce the effective surface area. The $[H_2O]$ relaxation data was consistent with a negligible paracellular water permeability in the MDCK cyst epithelium (see **Supplementary Methods**), suggesting that water movement via the paracellular pathway is not a significant factor[16].

AQP4 has been reported to be expressed in the basolateral membrane of principal cells in the renal collecting duct, in airways cell, the stomach, and the colon[11,18,19], as well as the end-feet of astrocytes[10,20]. However, we confirmed that WT-MDCK cysts did not express endogenous AQP4 under normal circumstances. In WT-MDCK cysts, the water permeability of the luminal membrane ($1.2 \pm 0.2 \times 10^{-3}$ cm/s) was similar to that measured previously in single Hela cells ($8.3 \pm 2.6 \times 10^{-4}$ cm/s)[13]. The mAQP4-MDCK cells formed cysts with enhanced expression of mAQP4 protein in the basolateral membrane (**Fig. 7B**), and in the H_2O/D_2O exchange experiment these cysts consistently showed ~3–4 -fold higher basolateral water permeability than the WT-MDCK cysts. Thus the mAQP4-MDCK cells

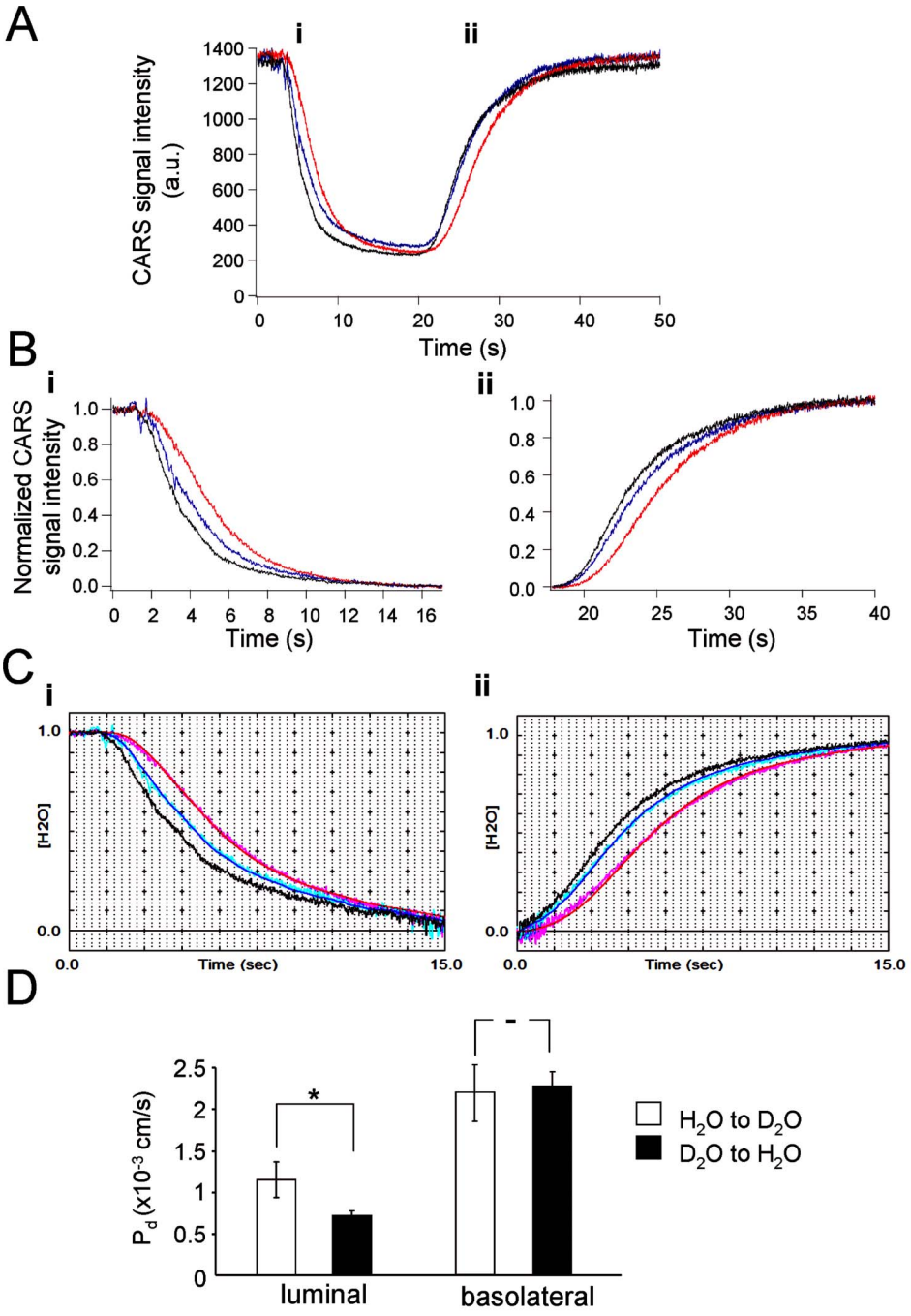

Figure 6 | Comparisons of the water permeability values estimated from the H_2O to D_2O switch and a sequential D_2O to H_2O switchback in the same cyst. (A) Raw CARS signal intensity data recorded on switching from an H_2O-based solution to a D_2O-based (i) solution and then subsequently switching the D_2O-based solution back to the H_2O-based solution (ii). (B) Normalized signal decays induced by (i) the H_2O to D_2O switch and (ii) the sequential D_2O to H_2O switchback. (C) Estimation of the water permeabilities (Pd) from the signal decays in (i) the H_2O to D_2O switch and (ii) the subsequent switchback shown in Fig. 6B. Note that the best-fitted curves are superimposed. (i) $P_d(l)$: 0.85×10^{-3} cm/s; $P_d(bl)$: 1.3×10^{-3} cm/s; $P_d(p)$: 10^{-7} cm/s. (ii) $P_d(l)$: 0.66×10^{-3} cm/s; $P_d(bl)$: 1.9×10^{-3} cm/s; $P_d(p)$: 10^{-7} cm/s. In the switch back experiment (Fig.S6C–ii), the whole [H_2O] data were used for the best-fit. (D) Summary data for the water permeabilities (Pd) obtained from the H_2O to D_2O switch and the sequential D_2O to H_2O switchback (performed on the same cyst). Mean ± SEM, n = 12 cysts. p = (luminal) 0.012 and (basolateral) 0.41 by a paired Wilcoxon rank test.

formed a polarized epithelium and expressed functional AQP4 water channels. Note that the successful mAQP4 transfection was checked by a co-expressed EGFP signal in the MDCK cell layer (**Fig. 7C**) prior to use in the CARS experiments. On the other hand, the stable over-expression of mAQP4 did not affect the luminal membrane water permeability significantly (**Fig. 7E**).

Finally, we were successful in making 'real-time' measurements of hormone-induced water permeability changes in M-1 cysts (**Fig. 8**). Working with M-1 cells was technically challenging as they formed smaller cysts with a more irregular shape compared to MDCK cells. In renal cortical collecting duct cells (the origin of M-1 cells), the water permeability of the basolateral membrane is high due to the expression of AQP4 and AQP3, one of the aquaglyceroporins[10], and not rate-limiting for transepithelial water transport. In the absence of AVP stimulation, the majority of the AQP2 is localized in intracellular vesicles and the luminal membrane water permeability is low.

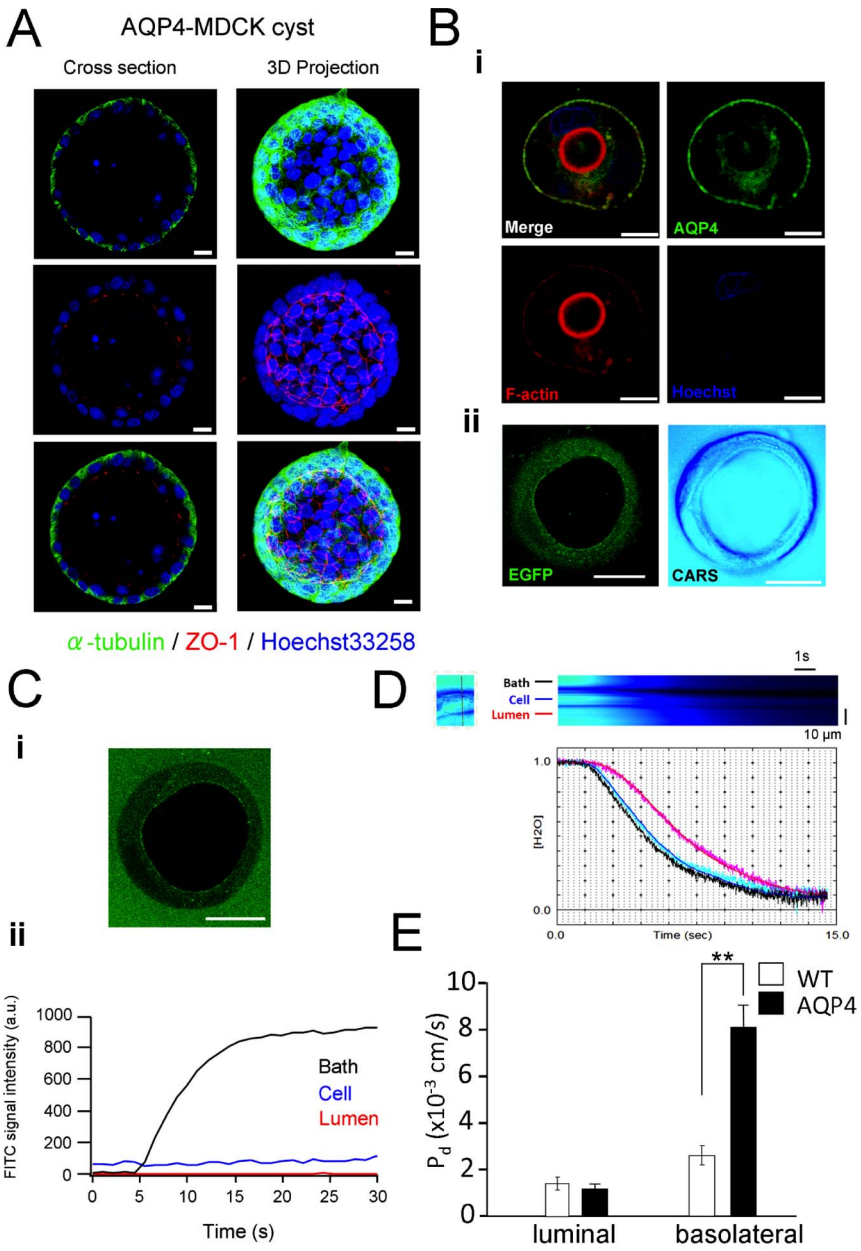

Figure 7 | Effects of AQP4 expression on water movement in MDCK cyst. (A) Cross section and 3D projection images of immuno-histochemical stained cysts from MDCK cells stably transfected with AQP4 (Day 5). (green) α-tubulin; (red) ZO-1; (blue) Hoechst33258. The scale bars indicate 10 μm. (B) Expression of AQP4 in AQP4-MDCK cysts. **(i)** Immnuo-staining of AQP4 in an AQP4 MDCK cyst. (green) AQP4; (red) F-actin; (blue) Hoechst33258. Scale bar: 10 μm. **(ii)** EGFP (left) and CARS (right) signals obtained from an AQP4 MDCK cyst on the CARS microscope. Note that the intracellular fluorescent signal comes from EGFP co-transfected with AQP4 by the mAQP4-M1-pIRES2-EGFP construct, not a leak in of FITC-dextran. Scale bar: 20 μm. (C) Representative example of a leak test in AQP4-MDCK cysts. **(i)** A fluorescent image of an AQP4-MDCK cyst 30 min after the application of 20-kDa FITC-dextran (5 mg/ml). Scale bar: 20 μm **(ii)** Time-course of the FITC signals in bath, cell and lumen after the FITC-dextran application. Note that the AQP4-WT cells also expressed EGFP and its fluorescent signal was also detected in the cell layer of the cyst. (D) Decay of the normalized H_2O concentration in bath, cell and lumen during the H_2O/D_2O exchange in an AQP4-transfected MDCK cyst. (Top panel) CARS line scanning data. 176 × 10385 pixels. 0.207 μm/pixel; 1.36 ms/line. (E) Summary data for the water permeability of the luminal and basolateral membranes in WT and AQP4-transfected MDCK cysts. Mean ± SEM, n = 15 (WT) and 8 (AQP4) separate cysts. p = (luminal) 0.9 and (basolateral) 0.005 by unpaired Wilcoxon rank test (**: $p < 0.005$).

AVP induces a redistribution of AQP2 to the luminal membrane and dramatically increases reabsorption of water from the urine. Although the M-1 cell is a cell-line, it has been reported to retain some of the physiological transport functions of the cortical collecting duct, e.g., vasopressin-stimulated Na^+ transport[21] and PGE2-stimulated Cl^- secretion[22] when reconstituted into monolayers. It was also reported that AVP induced a redistribution of AQP2 from intracellular vesicles to the plasma membrane in M-1 cells[17]. In this study, we detected an AQP2 signal on the luminal membrane of the M-1 cysts after a 30 min incubation with 100 nM AVP (**Fig. 8A**). Consistent with the AQP2 immunostaining data (**Fig. 8A**), our CARS experimental results (**Fig. 8C**) showed an AVP-induced increase in luminal diffusive water permeability by ~1.5-fold (**Fig. 8D**). The leak test showed that the tight junction of M-1 cysts is not permeable to 20-kDa FITC-dextran (**Fig. 8B**). In M-1 cysts, as well as MDCK cysts, water permeation via the paracellular pathway

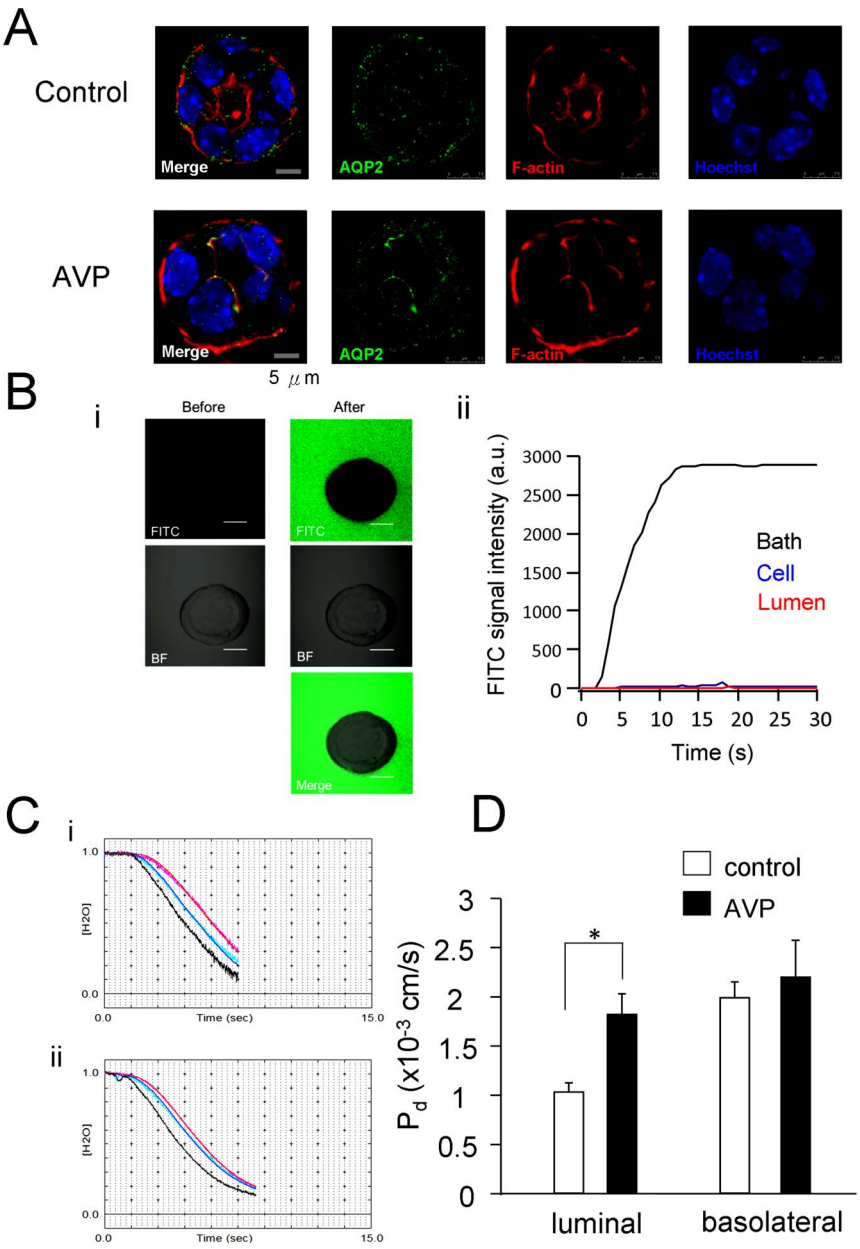

Figure 8 | Effects of vasopressin on water movement in an M-1 cyst. (A) Immuno-histochemical staining of AQP2 in M-1 cysts in control and after incubation with 100 nM arginine vasopressin (AVP) for 30 min at 37°C. (green) AQP2; (red) F-actin; (blue) Hoechst33258. (B) Leak test for M-1 cysts using FITC-dextran. **(i)** Fluorescent images of an M-1 cyst before and 30 min after the application of 1 ml 20-kDa FITC-dextran (5 mg/ml). Scale bar: 20 μm **(ii)** Time-course of the FITC signals in bath, cell and lumen after the FITC-dextran application to the M-1 cyst. (C) Plots of the normalized H_2O concentration in the bath, cell and lumen in the M-1 cyst following the H_2O to D_2O perfusion switch **(i)** before and **(ii)** after an application of vasopressin. $P_d(l)$: (i) 1.4×10^{-3} cm/s, (ii) 4.1×10^{-3} cm/s. $P_d(bl)$: (i) 1.9×10^{-3} cm/s, (ii) 2.0×10^{-3} cm/s. (D) Summary data for the water permeability of luminal and basolateral membranes in M-1 cysts before and after an application of vasopressin to the same cyst. Mean ± SEM, n = 8 cysts. $p =$ (luminal) 0.0078 and (basolateral) 0.84 by a paired Wilcoxon rank test (*$p < 0.01$).

was not significant when compared to water permeation via the transcellular route.

More than 50 years ago, Koefoed-Johnsen and Ussing[23] presented the two-membrane (luminal and basolateral) model of Na^+ transport by the frog skin. This idea has guided thinking throughout epithelial biology for the past half century and is now recognized as a milestone in membrane transport physiology[24]. However, lack of the methodology allowing a direct observation of water movement has prevented us from measuring luminal and basolateral water permeability separately until our present work.

The CARS method also allows us to observe the diffusive movement of water and not just the net water flow driven by either osmotic or hydrostatic pressure differences. Diffusive water movement is of biological significance because nutrients, paracrine hormones and growth factors are conveyed amongst and between cells, and through capillary vessels by very slow lymphatic and plasma flows respectively. Under these conditions, diffusive water movement is likely to dominate over net water flow driven by either osmotic or hydrostatic pressure gradients, because the interstitial flow velocities *in vivo* are too slow and heterogeneous (probably 0.1–4 μm/s or slower)[25]. It is also worthy to note that diffusive water dynamics are likely to be important in understanding the mechanism of fetal edema, e.g. traumatic cerebral edema and anaphylactic laryngeal edema.

To date, it has not been technically possible to measure microscopic diffusive water movements in the interstitial space of complex tissues and organs; so this area is completely unexplored. Therefore, we believe that the present study represents a milestone in the field of water transport and opens up a new field of cellular physiology; that is the study of microscopic diffusive water movement in the complex environment that exists within the extracellular space of the body's tissue and organs.

In this study, we have made the first, direct, observation of diffusive water movement using CARS microscopy by analyzing the CARS imaging data with a novel simulation model. This has allowed us to quantitatively characterize water homeostasis in a complex, structurally polarized tissue (an isolated epithelium), and also to detect changes in diffusive water permeability caused by hormonal stimulation. Finally, it should be noted that the CARS technique is not only applicable to transporting epithelia, but also to other physiologically and medically important tissues and organs, e.g., the microcirculation systems in the heart, brain, kidney and liver.

Methods

CARS microscopy. Imaging was performed using CARS microscopy as previously described[13]. In short, we obtained the CARS signal from H_2O molecules using an Olympus laser scanning microscope (FV1000/IX81, Olympus, Tokyo, Japan) into which a fundamental 1064 nm (9400 cm^{-1}) Stokes beam (7 ps, 76 MHz repetition rate; picoTRAIN Green & UV, IC-532-4000, High-Q, Rankweil, Austria) and a 793.6 nm (12600 cm^{-1}) pump beam generated by an optical parametric oscillator (OPO) (Levante Emerald, AP&E, GmbH, Berlin, Germany) were coupled and co-linearly introduced and focused onto a sample using a water immersion objective lens (UPlanSApo 60 XW, Olympus: 60×, numerical aperture (NA) = 1.2). The average (peak) laser power at the sample was ~30 mW (56.4 W) for the pump beam and ~15 mW (28.2 W) for the Stokes beam, which are comparable to the intensities used by others[4]. No morphological changes in the tissue were observed during the experiments. For CARS imaging, the forward-CARS signal was corrected via a custom-built forward detector via a condensing lens (IX2-LWUCD, NA0.55; Olympus) in the Olympus IX81 inverted microscope. Note that a non-resonant background signal was observed in the CARS D_2O images (e.g. **Fig. 3A**). We did not perform D_2O imaging (2400 cm^{-1}) experiments, although they are theoretically possible, because of a low signal-to-noise ratio in D_2O images obtained in our system.

We also performed single-photon fluorescence imaging using an argon 488 nm excitation laser. All the conventional confocal fluorescence imaging was performed on the CARS microscope system. We were able to obtain both the CARS and the confocal fluorescence signals using the same filter set-up by using a combination of a specially designed dichroic mirror which reflects pump (793.6 nm), Stokes (1064 nm) and the single-photon excitation (488 nm) beams, but transmits the green fluorescent signal, plus a confocal unit for the fluorescence-signal detection.

CARS imaging of H_2O/D_2O exchange process and data analysis. To detect the water diffusion in the cysts, we used two kinds of perfusion solutions: one was H_2O-based (all the solutes were dissolved in Milli-Q water; Millipore, Gradient A10™); the other was D_2O-based (dissolved in Deuterium oxide; Cambridge Isotope Laboratories Inc., DLM-2259-1, (D_2O 99.8%)). Both the H_2O and D_2O perfusion solutions contained (in mM): 140 NaCl, 5 KCl, 1 $MgCl_2$, 1 $CaCl_2$, 10 D-glucose, and 10 HEPES (pH 7.4 with 1N NaOH dissolved in H_2O and D_2O respectively). For each experiment, the culture medium was replaced with the H_2O-based extracellular solution at first. Then the external H_2O-based extracellular solution was fully switched to the D_2O-based extracellular solution using a gravity-feed perfusion system (H_2O to D_2O switching) (**Fig. 1A**).

The focal (x-y) image size is currently 52.633 μm × 52.633 μm with 512 × 512 pixels (0.103 μm/pixel). The lateral optical resolution of the CARS scanning images was about 500 nm (5 pixels). We employed a pixel size that would tend to oversample (~100–400 nm per pixel) so as to obtain the CARS signal from the quite thin cell layer, avoiding as far as possible scattering artifacts near the plasma membrane. The data acquisition time was 2 μs/pixel. The time resolution in the free run line scanning mode (x-t image) was ~ 0.5–1.6 ms/line dependent on the length of the scanning line.

Estimation of H_2O concentration from the CARS signal intensity. The raw CARS signal obtained from the PMT contained a non-resonant background signal as well as the CARS signal originating from H_2O molecules. Therefore, we employed the data processing procedure described below to calculate the H_2O concentration from the CARS signal intensity[26]:

1) To isolate the H_2O CARS signal from the non-resonant background signal, the steady state signal intensity reached after the bath solution was completely replaced with the D_2O-based solution (I_{D2O_full}) was subtracted from the CARS signal intensity data (I_{CARS}).
2) To compensate for the differences in optical conditions between the lumen, cell and bath, the CARS signal intensity was normalized to the steady state obtained when the bath was bathed with the H_2O-based solution (I_{H2O_full}).

$$I_{H2O} = \frac{I_{CARS} - I_{D2O\_full}}{I_{H2O\_full} - I_{D2O\_full}} \quad (1)$$

where I_{CARS} is the CARS signal intensity measured during the H_2O/D_2O exchange, I_{H2O_full} and I_{D2O_full} are the CARS signal intensities at a steady state with the H_2O- and D_2O-based solutions.

3) The normalized CARS signal intensity (I_{H2O}) was converted to the relative H_2O concentration using the calibration curve shown in Fig. 1C-ii. Note that the CARS signal intensities showed a nonlinear dependence on the change in H_2O concentration due to the intrinsic characteristics of the CARS process[2,3] The H_2O concentration was calculated by multiplying the relative H_2O concentration by 55 M, the concentration of H_2O in pure water.

$$[H_2O] = 55(M) \times (I_{H2O})^{1/1.67} \quad (2)$$

where I_{H2O} is the normalized CARS H_2O signal intensity.

Multi-shelled, three-compartment, model for studying the H_2O/D_2O exchange process in epithelial cysts. To investigate the diffusive water movement in the cysts from the CARS H_2O imaging data, we developed a three compartmented, concentric sphere, model in which each compartment is further divided into concentric spherical, thinner, sub-compartments (multi-shelled concentric sphere model: **Fig. 1B**) (see **Supplementary Methods** for detail).

To determine the diffusive water permeability in the luminal membrane, basolateral membrane and paracellular pathway from the cyst CARS imaging data, we developed an analysis program based on the best fit of the simulated water concentration changes in the cyst compartments to the experimental data (e.g., **Figs. 3B&5C**). Briefly, the analysis program reproduced the H_2O concentration in the lumen ($[H_2O]_{lumum}$) and the epithelium (cell layer) ($[H_2O]_{cell}$) from the experimental $[H_2O]$ data in the bath ($[H_2O]_{bath}$). Sequentially, the software compared the simulated and the experimental data for $[H_2O]_{lumen}$ and $[H_2O]_{cell}$ and found the parameter sets for minimizing the deviation between the experimental and simulated $[H_2O]_{lumen}$ and $[H_2O]_{cell}$ data (see **Supplementary Methods** for more detail).

Stable cell lines and cyst formation. MDCK and M-1 cell lines were purchased from RIKEN cell bank, Japan and sub-cultured according to ATCC (American Type Culture Collection) protocols. MDCK cells were maintained in DMEM containing 5 mM D-glucose, 100 U/ml penicillin G, 100 mg/ml streptomycin and 10% FBS. M-1 cells were maintained in a 1 : 1 mixture of Dulbecco's modified Eagle's medium and Ham's F12 medium containing 2.5 mM L-glutamine,15 mM HEPES, 0.5 mM sodium pyruvate, 1.2 g/L sodium bicarbonate, 5 μM dexamethasone and 5% fetal bovine serum.

To generate MDCK cell lines stably overexpressing mouse AQP4 (mAQP4), mAQP4 cDNA was subcloned into the pIRES2-EGFP vector and MDCK cells were stably transfected with mAQP4-M1-pIRES2-EGFP construct by using Lipofectamine 2000 (Invitrogen Life Technologies, Paisley, UK) according to the manufacturer's protocol. Then mAQP4/MDCK cells were selected using 200 μg/ml of G418 disulfate in aqueous solution (Nacalai tesqe, Inc. Tokyo Japan). After 10 days of the selection, colonies were isolated and picked, and each colony was grown and expanded in separated wells. The mAQP4 expression quality was confirmed by western blot and confocal immunofluorescence microscopy.

MDCK cysts and M-1 cysts were formed in a 3D growth medium containing Matrigel (BD Biosciences, Bedford, MA). Single-cell suspensions at 0.25 ~ 1 × 10^5 cells/ml were mixed with 2% Matrigel and seeded onto order-made dishes with an small oval (4 × 10 mm) glass bottom area at the center of a 35 mm dish (Matsunami, Osaka, Japan. Glass thickness: 0.08–0.12 mm). After culturing at 37°C for 5–7 days, mature cysts were formed and used for the experiments.

Immunohistochemistry. Primary antibodies utilized were: rabbit polyclone anti-mAQP4 (Sigma Aldrich), goat anti-AQP2 (G19, Santa Cruz Biotechnology), rabbit anti-β-catenin (H-102; Santa Cruz Biotechnology, Santa Cruz, CA), rat anti-zonula occludens (ZO)-1 (R40-76; Santa Cruz Biotechnology, Santa Cruz, CA), mouse α-tubulin (B5-1-2; Santa Cruz Biotechnology, Santa Cruz, CA), and rabbit β-actin (H-300; Santa Cruz Biotechnology, Santa Cruz, CA). Secondary antibodies utilized were anti-mouse Alexa Fluor 488, anti-rabbit 555, and anti-rat 647 (Invitrogen). Actin filaments were stained with Texas red-phalloidin (Invitrogen). Nuclei were stained with Hoechst 33258 (Invitrogen).

Cyst samples were fixed with 4% paraformaldehyde for 30 mins. After extensive washing, the cysts were blocked with 10% FBS in PBST for 30 mins, and then incubated with the primary antibodies at 4°C for overnight. After washing, cells were incubated in Alexa Fluor-conjugated secondary antibodies for 1 h at room temperature. Samples were kept in PBS after washing and observed with a SP5 Leica confocal laser microscope. Images were analyzed with LAS AF Lite software (Leica Microsystems, Wetzlar, Germany).

Immuno-histochemical staining of cysts formed by WT-MDCK cells and MDCK cells stably transfected with mAQP4 was performed to see the 3D structure of the cell membrane (stained by α−tubulin) and the nuclei (stained by Hoechst 33258) (**Figs. 2A&7A**). Also the immuno-histochemical staining of ZO-1 was performed to confirm the network of pentagonal and hexagonal frames, suggesting that the tight junction is correctly formed between the MDCK cells (**Figs. 2A&7A**).

The stable transfection of mAQP4 induced the expression of mAQP4 on the basolateral membrane of the cysts (**Fig. 7B**). The mAQP4-M1-pIRES2-EGFP construct was used as a marker for successful mAQP4 transfection (**Fig. 7C**), and all cysts were checked for an EGFP signal in the MDCK cell layer prior to use in the CARS experiments.

Leak test for the cysts. The immunostaining data suggested that both MDCK and M-1 cells formed complete cysts which contained a polarized epithelium. For the CARS experiments, we selected complete cysts by observation under bright field optics. To confirm the formation of complete cysts, especially the intactness of the tight junction, we performed a leak test which involved adding a fluorescein isothiocyanato conjugated with dextran (FITC-dextran) to the bath after each CARS experiment and checked whether the FITC signal appeared in the lumen. FITC-dextran is a hydrophilic large (4–20 kDa or larger) compound, which does not permeate the plasma membrane and is widely used as an indicator for a significant bath – lumen shunt[27,28]. The absence of a luminal FITC signal, even 30 min after the addition of FITC-dextran to the bath solution, was taken to indicate that the cyst had formed functional tight junctions (**Figs. 2B**, **7C&8B**).

Statistics. Statistical analysis was performed using Igor Pro (Wavemetrics, Inc., OR, USA). Normality was determined using the Kolmogorov-Smirnov test and then statistical comparisons were made using Wilcoxon rank test between two different groups. P-values of 0.05 or less were considered statistically significant.

1. Baker, M. Laser tricks without labels. *Nat. Methods* **7**, 261–266 (2010).
2. Cheng, J. X. Coherent anti-Stokes Raman scattering microscopy. *Appl. Spectrosc.* **61**, 197–208 (2007).
3. Evans, C. L. & Xie, X. S. Coherent anti-stokes Raman scattering microscopy: chemical imaging for biology and medicine. *Annu. Rev. Anal. Chem. (Palo Alto Calif)* **1**, 883–909 (2008).
4. Freudiger, C. W. *et al*. Label-free biomedical imaging with high sensitivity by stimulated Raman scattering microscopy. *Science* **322**, 1857–1861 (2008).
5. Okuno, M., Kano, H., Leproux, P., Couderc, V. & Hamaguchi, H. O. Ultrabroadband multiplex CARS microspectroscopy and imaging using a subnanosecond supercontinuum light source in the deep near infrared. *Opt. Lett.* **33**, 923–925 (2008).
6. Rinia, H. A., Burger, K. N., Bonn, M. & Muller, M. Quantitative label-free imaging of lipid composition and packing of individual cellular lipid droplets using multiplex CARS microscopy. *Biophys. J.* **95**, 4908–4914 (2008).
7. Le, T. T., Yue, S. & Cheng, J. X. Shedding new light on lipid biology with coherent anti-Stokes Raman scattering microscopy. *J. Lipid Res.* **51**, 3091–3102 (2010).
8. Potma, E., de Boeij, W. P., van Haastert, P. J. & Wiersma, D. A. Real-time visualization of intracellular hydrodynamics in single living cells. *Proc. Natl. Acad. Sci. U S A* **98**, 1577–1582 (2001).
9. Preston, G. M., Carroll, T. P., Guggino, W. B. & Agre, P. Appearance of water channels in Xenopus oocytes expressing red cell CHIP28 protein. *Science* **256**, 385–387 (1992).
10. Agre, P. *et al*. Aquaporin water channels--from atomic structure to clinical medicine. *J. Physiol.* **542**, 3–16 (2002).
11. Verkman, A. S., Matthay, M. A. & Song, Y. Aquaporin water channels and lung physiology. *Am. J. Physiol. Lung Cell Mol. Physiol.* **278**, L867–879 (2000).
12. Verkman, A. S. Water permeability measurement in living cells and complex tissues. *J. Membr. Biol.* **173**, 73–87 (2000).
13. Ibata, K., Takimoto, S., Morisaku, T., Miyawaki, A. & Yasui, M. Analysis of aquaporin-mediated diffusional water permeability by coherent anti-stokes Raman scattering microscopy. *Biophys. J.* **101**, 2277–2283 (2011).
14. Madin, S. H. & Darby, N. B., Jr. Established kidney cell lines of normal adult bovine and ovine origin. *Proc. Soc. Exp. Biol. Med.* **98**, 574–576 (1958).
15. Stoos, B. A., Naray-Fejes-Toth, A., Carretero, O. A., Ito, S. & Fejes-Toth, G. Characterization of a mouse cortical collecting duct cell line. *Kidney Int.* **39**, 1168–1175 (1991).
16. Kovbasnjuk, O., Leader, J. P., Weinstein, A. M. & Spring, K. R. Water does not flow across the tight junctions of MDCK cell epithelium. *Proc. Natl. Acad. Sci. U S A* **95**, 6526–6530 (1998).
17. Goel, M., Sinkins, W. G., Zuo, C. D., Hopfer, U. & Schilling, W. P. Vasopressin-induced membrane trafficking of TRPC3 and AQP2 channels in cells of the rat renal collecting duct. *Am. J. Physiol. Renal Physiol.* **293**, F1476–1488 (2007).
18. Ma, T. & Verkman, A. S. Aquaporin water channels in gastrointestinal physiology. *J. Physiol.* **517 (Pt 2)**, 317–326 (1999).
19. Frigeri, A., Gropper, M. A., Turck, C. W. & Verkman, A. S. Immunolocalization of the mercurial-insensitive water channel and glycerol intrinsic protein in epithelial cell plasma membranes. *Proc. Natl. Acad. Sci. U S A* **92**, 4328–4331 (1995).
20. Yukutake, Y. & Yasui, M. Regulation of water permeability through aquaporin-4. *Neuroscience* **168**, 885–891 (2010).
21. Nakhoul, N. L., Hering-Smith, K. S., Gambala, C. T. & Hamm, L. L. Regulation of sodium transport in M-1 cells. *Am. J. Physiol.* **275**, F998–F1007 (1998).
22. Sandrasagra, S., Cuffe, J. E., Regardsoe, E. L. & Korbmacher, C. PGE2 stimulates Cl- secretion in murine M-1 cortical collecting duct cells in an autocrine manner. *Pflugers Arch.* **448**, 411–421 (2004).
23. Koefoed-Johnsen, V. & Ussing, H. H. The nature of the frog skin potential. *Acta Physiol. Scand.* **42**, 298–308 (1958).
24. Palmer, L. G. & Andersen, O. S. The two-membrane model of epithelial transport: Koefoed-Johnsen and Ussing (1958). *J. Gen. Physiol.* **132**, 607–612 (2008).
25. Rutkowski, J. M. & Swartz, M. A. A driving force for change: interstitial flow as a morphoregulator. *Trends Cell Biol.* **17**, 44–50 (2007).
26. Akimov, D. *et al*. Different contrast information obtained from CARS and nonresonant FWM images. *J. Raman Spectrosc.* **40**, 941–947 (2009).
27. Hoffmann, A. *et al*. High and Low Molecular Weight Fluorescein Isothiocyanate (FITC)-Dextrans to Assess Blood-Brain Barrier Disruption: Technical Considerations. *Transl. Stroke Res.* **2**, 106–111 (2011).
28. Tafazoli, F., Zeng, C. Q., Estes, M. K., Magnusson, K. E. & Svensson, L. NSP4 enterotoxin of rotavirus induces paracellular leakage in polarized epithelial cells. *J. Virol.* **75**, 1540–1546 (2001).

Acknowledgements

This work was supported by Global Center of Excellence Program for Humanoid Metabolomic Systems Biology in the Ministry of Education, Culture, Sports, Science and Technology (MEXT) of Japan (Y.C.Y., M.Y.), Strategic International Research Cooperative Program, Japan Science and Technology Agency (JST) (M.Y.), Keio University Program for the Advancement of Next Generation Research Projects (M.Y.) and Keio Gijuku Fukuzawa Memorial Fund for the Advancement of Education and Research (Y.S.). The authors appreciate Dr. Atsushi Miyawaki, RIKEN, Japan for his useful intensive discussions, Dr. Manabu Kubokawa, Iwate Medical University, Japan for helpful suggestions, Mr. Zifang Zhao, Peking University for the MATLAB programing and Professor B.E. Argent, Newcastle University, U.K. for critical reading of the manuscript.

Author contributions

M.Y. organized the project. Y.S. designed the research. Y.C.Y., Y.S. and T.M. performed the experiments. S.T. contributed the nonlinear optical microscopy. Y.S. developed the new analytic tools. Y.S. and Y.C.Y. analyzed the data. Y.S., M.Y. and Y.C.Y. wrote the manuscript.

Additional information

Supplementary information accompanies this paper at http://www.nature.com/scientificreports

Competing financial interests: The authors declare no competing financial interests.

How to cite this article: Yu, Y., Sohma, Y., Takimoto, S., Miyauchi, T. & Yasui, M. Direct visualization and quantitative analysis of water diffusion in complex biological tissues using CARS microscopy. *Sci. Rep.* **3**, 2745; DOI:10.1038/srep02745 (2013).